TITLE: Behaviour of grout-filled double-skin tubular steel stub-columns: Numerical modelling and design considerations

AUTHORS

Nikolaos I. Tziavos[a], Michaela Gkantou[b], Marios Theofanous[c], Samir Dirar[c], Charalampos Baniotopoulos[c]

Corresponding author: Nikolaos I. Tziavos

Email: nt431@cam.ac.uk

Affiliations

[a]Centre for Smart Infrastructure and Construction, Department of Engineering, University of Cambridge, UK

[b]Department of Civil Engineering, Liverpool John Moores University, UK

[c]Department of Civil Engineering, University of Birmingham, UK

Number of figures: 13

Number of tables: 5

Nomenclature

A_g	Cross sectional area of grout core
A_k	Cross sectional area of hollow part
A_{so}	Cross sectional area of outer steel tube
A_{si}	Cross sectional area of inner steel tube
D_o	External tube diameter
D_i	Internal tube diameter
D_g	Grout core diameter
f_{syo}	External steel yield strength
f_{syi}	Internal steel yield strength
f_{sy}	Steel yield strength
f_{rp}	Lateral confining pressure
f_{gt}	Grout tensile strength
f_{gc}	Compressive strength of grout
f_{cu}	Compressive strength of cubic sample
f_c	Compressive cylinder strength
f'_{cc}	Confined compressive strength
f'_c	Unconfined compressive strength
L	Stub-column length
a	Steel ratio
a_n	Nominal steel ratio
t_o	External tube thickness
t_i	Internal tube thickness
β_c	Post-peak confinement factor
γ_c	Strength reduction factor
ε'_{cc}	Strain corresponding to confined compressive strength
$\bar{\lambda}$	Relative slenderness
ξ	Confinement factor
χ	Hollow ratio, $\chi = \frac{D_i}{D_o - 2t_o}$

ABSTRACT

The use of grout-filled double-skin tubular (GFDST) sections in civil, bridge and offshore engineering applications is rapidly increasing. The design of such composite members is not directly covered by design codes, despite recent research studies investigating their performance, proposing design equations or modifying existing codified methods. Aiming to extend the available pool of structural performance data, the current study reports the results of an extensive numerical investigation on GFDST stub-columns. Finite element (FE) models, are developed and validated against published test data. A parametric investigation is conducted to evaluate the effect of key parameters, including cross-sectional slenderness, hollow ratio and the effect of concrete infill on the capacity of GFDST members. The numerically obtained load capacities along with collated test data are utilised to assess the applicability of design strength predictions based on European Code (EC4), the American Concrete Institute (ACI) and the analytical models proposed by Han et al. and Yu et al. Overall, the modified Yu et al. provided strength predictions with low scatter, whereas ACI yielded overly conservative predictions particularly for smaller hollow ratios.

Keywords: Composite columns, Double skin, Grout-filled, Finite element modelling

Highlights

- Numerical investigations on the performance of circular grout-filled double skin stub-columns.
- A parametric study was carried out to evaluate the influence of hollow ratio for varying cross sections on the compressive resistance.
- Assessment of codified methods and analytical models was performed.

1. Introduction

Concrete-filled tubular members are extensively employed in the construction of bridges, high-rise buildings, transmission towers and offshore structures [1, 2]. The surrounding tube provides confinement to the concrete core thus increasing its strength and ductility, whilst the concrete infill prolongs the occurrence of local buckling of the steel tube [3, 4]. Hence, they possess superior stiffness, strength and ductility compared to their bare steel or reinforced concrete counterparts resulting in smaller section sizes and larger lettable areas in the lower stories of multi-storey buildings [5]. In recent years, concrete-filled double skin tubular (CFDST) sections – where concrete is used to fill the annulus of two steel hollow sections, are attracting more interest, offering a lighter-weight alternative with enhanced stiffness, greater bending capacity, along with improved fire and seismic resistance [6-10].

In offshore construction, the infill material is typically a cement-based grout, resulting in grout-filled double skin tubular (GFDST) members. Such members are typically employed in oil and gas jacket platforms and offshore wind turbine foundations to form grouted connections [11] or as a remediation solution for lifetime extension as offshore structures in the North Sea are close to end-of-life [12]. Tubular double-skin filled members combining carbon and stainless steel [13, 14] are also used in submarine pipelines [13]. For offshore applications, GFDSTs with circular hollow sections (CHSs) are the configuration attracting more interest, as they provide the highest level of confinement on the sandwiched grout core [9, 15].

To better understand the response of this type of composite members, several researchers have experimentally investigated the strength of CFDST stub-columns and beam-columns with CHS tubes [6, 16-21]. The performance of different cross section shapes has also been evaluated in experimental studies, including CFDST with square hollow sections [22], rectangular hollow sections [23] and a combination of CHS and square hollow sections [16]. Han et al. [24] tested CFDST beam-columns with CHS and square cross-section under cyclic loads, whereas impact [25] and torsional tests [26] are also reported in the literature. Alternatives to carbon steel have been considered for structural applications in corrosive environments such as stainless steel [27-29] and aluminium [30], while the use of alternative cementitious composites such as rubberised concrete [31] has been urged by the need to minimise carbon emissions. Along with the aforementioned studies and to enhance the design practice of double-skinned composite members, researchers have conducted numerical investigations on the influence of material and geometrical parameters to generate new data and assess existing design methods [10, 13, 32-35].

Tests on GFDST members are scarce; Li et al. [12] reported 8 tests on stub-columns, 4 beam-columns and 2 on GFDST beams. Although the behaviour of the grout is often treated in a similar manner to that of concrete, for GFDSTs the grouted annulus is often very small resulting in higher hollow ratio (χ) values. Hollow ratio is the ratio of the internal steel diameter to the internal diameter of the external steel tube and is a commonly used metric in CFDSTs to provide information on the

cross-sectional geometry. Typical hollow ratios in previous experimental studies range from 0.2 to 0.7, whereas in offshore construction of GFDST, members with hollow ratios greater than 0.8 are often employed. The ultimate strength of GFDST stub columns, is a function of the steel yield strength (f_{sy}), the grout material compressive strength (f_{gc}) and the steel cross sectional properties (diameter to thickness ratio, D/t).

The present paper aims to fill this gap of limited available data on the structural performance of GFDST cross-sections across a range of hollow ratios by generating new data on the compressive capacity of GFDST stub columns by means of numerical modelling. Initially, the developed FE models are validated against experiments and subsequently a parametric study is carried out, investigating the effect of cross-sectional slenderness in small and large-diameter GFDST stub-columns. The hollow ratios for the developed FE models range from 0.4 to 0.9. The numerically obtained strengths are subsequently compared with design strength predictions obtained from European Code EN 1994-1-1 (EC4) [36], American Concrete Institute (ACI) [37] and the analytical models proposed by Han et al. [8] and Yu et al. [38].

2. Numerical modelling

The general-purpose FE software Abaqus [39] was employed for the numerical computations. In order to verify the accuracy of the numerical simulations, the numerical model was validated against test data reported in two experimental studies [6, 12], which are briefly discussed in Section 2.1. Sections 2.2 and 2.3 provide a detailed description on the numerical modelling assumptions, including the type of analyses, the adopted boundary conditions, interaction properties and the employed material models for the steel and the infill.

2.1 Selected experimental tests

The experiments on stub columns reported by Tao et al. [6] and Li et al. [12] are used herein to validate the FE models. The infill material in the tests reported in [6] is concrete with a compressive strength of 47.4 N/mm^2, whereas a grout infill with a compressive strength of 51.1 and 54.8 N/mm^2 was used in the tests reported in [12]. A total of 7 cross-section geometries were considered, with duplicate tests performed for each configuration thereby resulting in 14 experimental tests. The hollow ratio of the selected experimental tests ranges from 0.28 to 0.84. The dimensions of each specimen and the corresponding material properties are reported in Table 1, where L is the length of the specimen and D_o, t_o, D_i, t_i, the diameter and thickness of the external and internal steel tube respectively. A typical GFDST cross-section is shown in Figure 1, where A_{so} and A_{si} are the cross-sectional areas of the outer and the inner tube respectively, A_g the cross-sectional area of the grout and A_k the area of the hollow part. The average yield strength of the external (f_{syo}) and internal steel tubes (f_{syi}), as obtained from

tensile coupon tests, along with the cubic compressive strength (f_{cu}) and the recorded ultimate compressive strength ($P_{u,test}$) are also reported in Table 1.

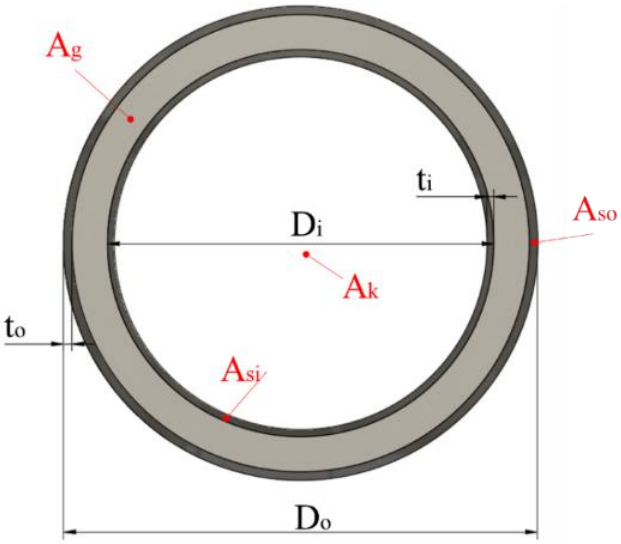

Figure 1: Geometric properties and notation for GFDST members

Table 1: Dimensions and material properties of circular double skin stub-column specimens used in the validation study

		Dimensions (mm)					Material properties			
Source	Test ID	D_o	t_o	D_i	t_i	L	f_{syo} (N/mm^2)	f_{syi} (N/mm^2)	f_{cu} (N/mm^2)	$P_{u,test}$ (kN)
[6]	cc2a	180	3	48	3	540	275.9	396.1	47.4	1790
	cc2b	180	3	48	3	540	275.9	396.1	47.4	1791
	cc3a	180	3	88	3	540	275.9	370.2	47.4	1648
	cc3b	180	3	88	3	540	275.9	370.2	47.4	1650
	cc4a	180	3	140	3	540	275.9	342	47.4	1435
	cc4b	180	3	140	3	540	275.9	342	47.4	1358
	cc5a	114	3	58	3	342	294.5	374.5	47.4	904
	cc5b	114	3	58	3	342	294.5	374.5	47.4	898
[12]	GC1-1	140	2.5	114	2	420	307	321	51.1	751.80
	GC1-2	140	2.5	114	2	420	307	321	51.1	698.86
	GC2-1	140	2.5	76	1.6	420	307	321	51.1	935.81
	GC2-2	140	2.5	76	1.6	420	307	321	51.1	928.62
	GCL-1	450	8	400	8	700	365	363	54.8	8867.92
	GCL-2	450	8	400	8	700	365	363	54.8	8735.85

2.2 Modelling assumptions

The loading and support conditions used in the experimental set-up were reflected in the boundary conditions and constraints adopted in the FE models. The boundary conditions were applied to two reference points, one on each end of the member, to which the degrees of freedom of the nodes of top and bottom cross-section of the model were tied. For each of the modelled tests the employed boundary conditions and constraints are shown in Figure 3a. Translation along the z-axis (i.e. parallel to the member axis) was allowed at the top reference points, with all remaining degrees of freedom restrained at both reference points. The FE models were based on the reported dimensions [6, 12] and

the steel and grout parts were discretised using linear solid elements with reduced integration (C3D8R). A mesh convergence study has been initially performed and a minimum of three elements have been used along the thickness of the steel plates and grout [40], respectively, as shown in Figure 3b, to produce accurate and computationally efficient results.

A quasi-static explicit solution scheme was selected in order to avoid convergence difficulties arising during the conventional implicit analysis due to the non-monotonic nature of the concrete response [41]. This approach alleviates convergence issues, however it is sensitive to the selected loading rate requiring engineering judgment on the computational results.

In this case, the step time was set at 10 s and a sufficiently small time increment was selected (10^{-4}) through a sensitivity analysis, ensuring that the inertia effects and artificial strain energy were negligible during the simulations. This was subsequently verified by ensuring that the kinetic energy remained smaller than 2% of the internal strain energy throughout the analysis. As an example this is illustrated in Figure 2. The load was applied using displacement control with a smooth amplitude function. Contact at the steel-grout interfaces was modelled using the general contact algorithm. In the normal direction, a hard contact formulation was chosen and a friction coefficient (μ) of 0.4 was assigned for the tangential direction [41].

Geometric imperfections and residual stresses are known to affect the response of axially loaded compressive tubular members. However, in GFDST members their influence is considerably reduced due to the presence of the infill material providing lateral restraint, which lessens the sensitivity of the tubes to local buckling and can therefore be ignored in the numerical analysis. This is in line with past studies [27] and as shown in Section 3, this assumption did not have any implication on the accuracy of the FE models.

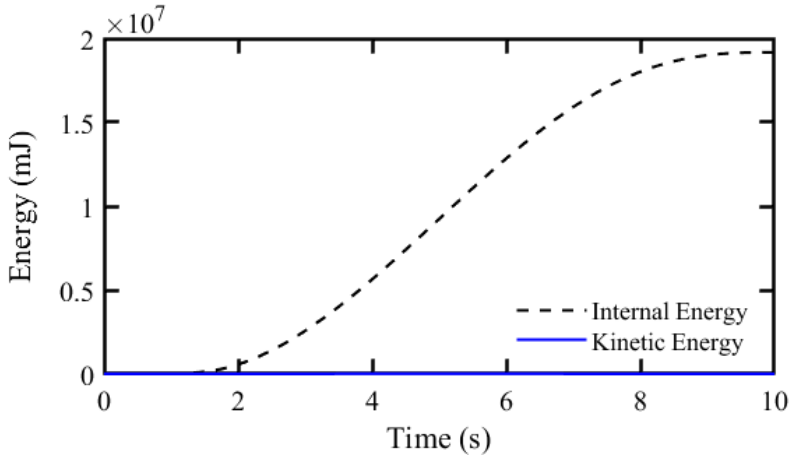

Figure 2: Comparison between internal and kinetic energy for specimen cc4a, b

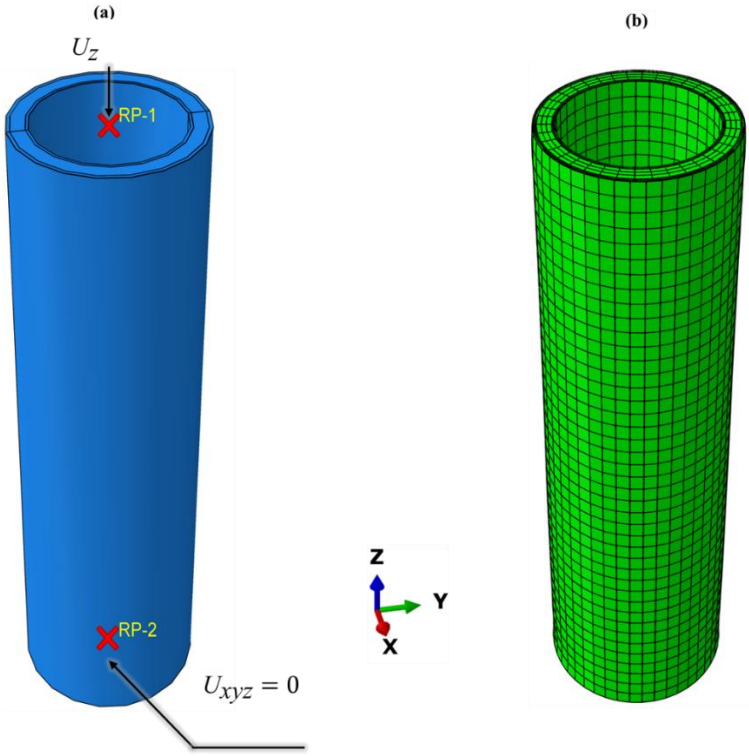

Figure 3: a) Boundary conditions on stub column finite element model and b) Typical mesh discretisation

2.3 Material modelling

For the steel tubulars the von Mises yield criterion with an isotropic hardening behaviour was used. The behaviour of the steel tubes was defined with a multi-linear stress-strain curve employing the yield and ultimate stress values and corresponding strains, which were experimentally obtained and reported in [12]. Cold-formed steel tubes were used in the experiments conducted by Tao et al. [6]. The yield strength for each steel section is given in Table 1, whereas the Poisson's ratio (v) was set at 0.3. The engineering stress (σ_{eng}) and strain (ε_{eng}) values were converted to true stress (σ_{true}) and strain (ε_{true}) following equations (1) and (2):

$$\sigma_{true}=\sigma_{eng}(1+\varepsilon_{eng}) \quad (1)$$

$$\varepsilon_{true}=\ln(1+\varepsilon_{eng}) - (\frac{\sigma_{true}}{E}) \quad (2)$$

Typical cement-based grouts exhibit similar behaviour to concrete in compression, although a larger scatter is to be expected in test results. For this purpose, for the subsequent analyses an analytical concrete model has been employed to describe the behaviour of the infill material in compression. In addition, to account for the restraint on the core from the steel tubes, a confined concrete model described in Ref. [15] was selected. An exemplary stress-strain curve when using the aforementioned analytical model is depicted in Figure 4 comprising three stages and is described herein. The first part of the confined stress-strain curve (AB) is described by equation (1), which was suggested by Mander et al. [42].

$$\sigma_c=\frac{f'_{cc}\lambda(\varepsilon_{cc}/\varepsilon'_{cc})}{\lambda-1+(\varepsilon_c/\varepsilon'_{cc})^{\lambda}} \quad , \varepsilon_c<\varepsilon'_{cc} \tag{3}$$

$$\text{where} \quad \lambda=\frac{E_c}{E_c-(f'_{cc}/\varepsilon'_{cc})} \tag{4}$$

193 and f'_{cc}, ε'_{cc} are the confined compressive strength and corresponding strain, ε_c the compressive strain
194 and E_c the Young's modulus. In this study the experimentally defined Young's modulus, reported in
195 [12] is used in the numerical models.

$$f'_{cc}=\gamma_c f'_c+k_1 f_{rp} \tag{5}$$

$$\varepsilon'_{cc}=\varepsilon'_c\left(1+k_2\frac{f_{rp}}{\gamma_c f'_c}\right) \tag{6}$$

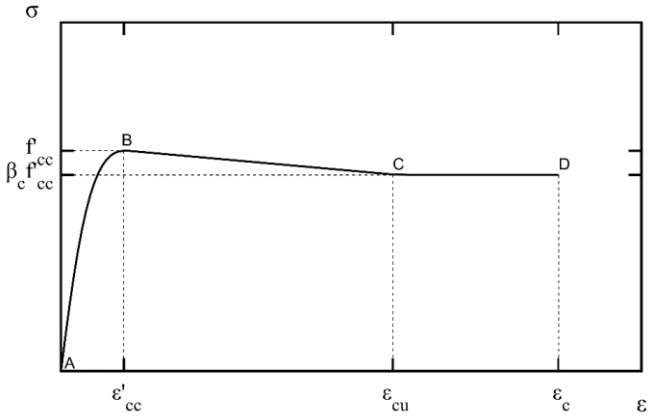

196

197 Figure 4: Exemplary stress-strain curve for confined concrete

198 For the constants k_1 and k_2, values of 4.1 and 20.5 as suggested in Richart et al. [43] were used, whereas
199 ε'_c is the unconfined concrete strain at f'_c and γ_c a strength reduction factor to account for material
200 imperfections and D_g is the diameter of the grout core. The lateral confining pressure (f_{rp}), on the grout
201 is obtained from equation (9) as it satisfies the cross-sections under investigation.

$$\varepsilon'_c=0.002+\left(\frac{\gamma_c f'_{cc}-28}{5400}\right),\ 28\le\gamma_c f'_c\le 82 \tag{7}$$

$$\gamma_c=1.85D_g^{-0.135},\ 0.85\le\gamma_c\le 1.0 \tag{8}$$

$$f_{rp}=\left(0.006241-0.0000357\frac{D}{t}\right)f_{syo},\ 47\le D/t\le 150 \tag{9}$$

202 The second (BC) and third (CD) stages of the stress-strain curve are described by equations (10) and
203 (11) respectively.

$$\sigma_c=\beta_c f'_{cc}+\left(\frac{\varepsilon_{cu}-\varepsilon_c}{\varepsilon_{cu}-\varepsilon'_{cc}}\right)\left(f'_{cc}-\beta_c f'_{cc}\right),\ \varepsilon'_{cc}\le\varepsilon_c\le\varepsilon_{cu} \quad (10)$$

$$\sigma_c=\beta_c f'_{cc},\ \varepsilon_c>\varepsilon_{cu} \quad (11)$$

where β_c accounts for any confinement after the peak load was reached and was expressed in [44] as follows:

$$\beta_c=0.0000339+\left(\frac{D}{t}\right)^2-0.10085\left(\frac{D}{t}\right)+1.3491 \quad (12)$$

Subsequently, the analytical compressive stress-strain curve was converted to true values and employed in the finite element model with the Concrete Damaged Plasticity model. In this study, following a sensitivity analysis, a dilation angle equal to 20° was found to result in good agreement with the experimental tests. For the remaining parameters, the eccentricity was set equal to 0.1, the ratio of equibiaxial to uniaxial compressive stress f_{b0}/f_{c0} was taken equal to 1.16 and finally the ratio of the second stress invariant on the tensile meridian to that on the compressive meridian at initial yield was set equal to 0.725 as per [45]. The tensile strength of the grout was estimated from equation (13) as suggested in [46] and a stress-displacement curve was defined for the tensile response of the infill material.

$$f_{gt}=0.3\left(f_{ck}\right)^{2/3} \quad (13)$$

3. Validation

The FE models were verified against the experimental tests reported in Refs. [6, 12]. The comparison between the tests and the numerical models was based on the load-displacement response, the observed failure modes and the ultimate axial capacity. In Figure 5 the experimental and the numerical load – axial displacement response is compared. The initial stiffness has been accurately simulated in all the examined cases, demonstrating that the elastic constants and boundary conditions were accurately modelled. In all the models the ultimate load is also well captured. The ultimate load ($P_{u,\ test}$), is compared with the numerically-obtained one ($P_{u,\ FE}$) in Table 2, showing very good agreement, with an average ratio of 1.018 and a COV of 0.033. Typical buckling modes in filled double-skin members include outward buckling of the external tube, inward/outward buckling of the internal tube and crushing/cracking of the infill medium. This is confirmed in Figure 6, where a comparison of the experimental and numerical failure modes is made. The observed outward buckling of the external and internal steel tubes and grout/concrete crushing is accurately captured for different models. As shown in Figure 5, the post-peak behaviour which was recorded in some of the experiments has not been very well captured by the numerical model, which is possibly attributed to the employed analytical concrete model and the plateau it forms until it reaches the ultimate strain, as illustrated in Figure 4 and was also

suggested by Thai et al. [47]. It is considered that this did not have any impact on the primary focus of this paper, i.e. the ultimate load that has been captured with great precision. Overall, it is demonstrated that from the validation study the numerical models provide an accurate representation of the real conditions and a precise prediction of the experimentally observed ultimate load and corresponding failure modes which are subsequently used for the analytical assessment.

Table 2: Comparison of ultimate strength of FE models against test results

Source	Test ID	$P_{u,\,test}$ (kN)	$P_{u,\,FE}$ (kN)	$P_{u,\,test/FE}$
Tao et al. [6]	cc2a	1790	1780.19	1.005
	cc2b	1791	1780.19	1.006
	cc3a	1648	1668.61	0.987
	cc3b	1650	1668.61	0.988
	cc4a	1435	1311.05	1.094
	cc4b	1358	1311.05	1.035
	cc5a	904	854.54	1.057
	cc5b	898	854.54	1.050
Li et al. [12]	GC1-1	751.80	731.10	1.028
	GC1-2	698.86	731.10	0.956
	GC2-1	935.81	933.60	1.002
	GC2-2	928.62	933.60	0.995
	GCL-1	8867.92	8622.52	1.028
	GCL-2	8735.85	8622.52	1.013
Average				**1.017**
COV				**0.033**

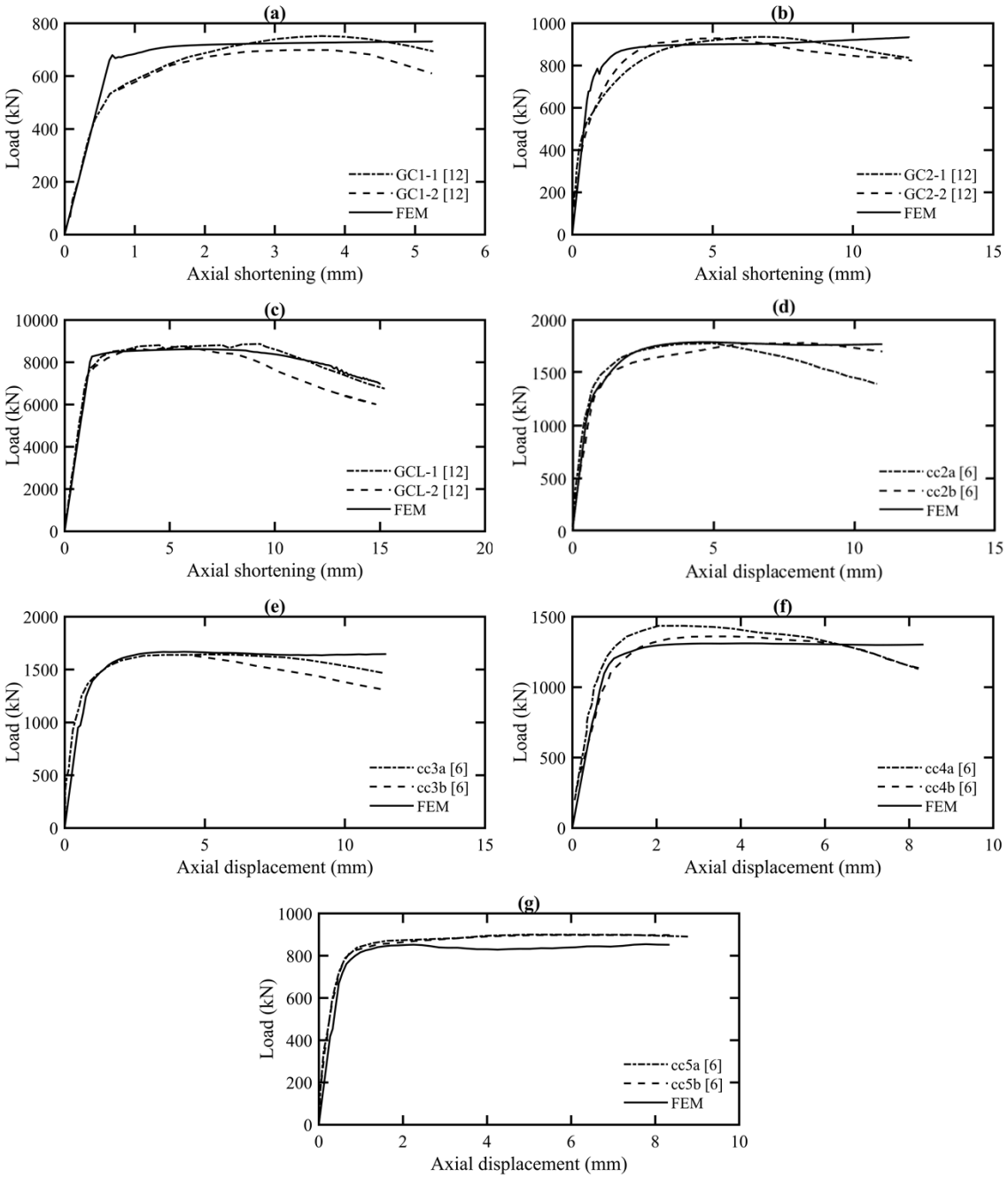

Figure 5: Comparison of axial load-shortening curves for experimental and FE models for stub-columns

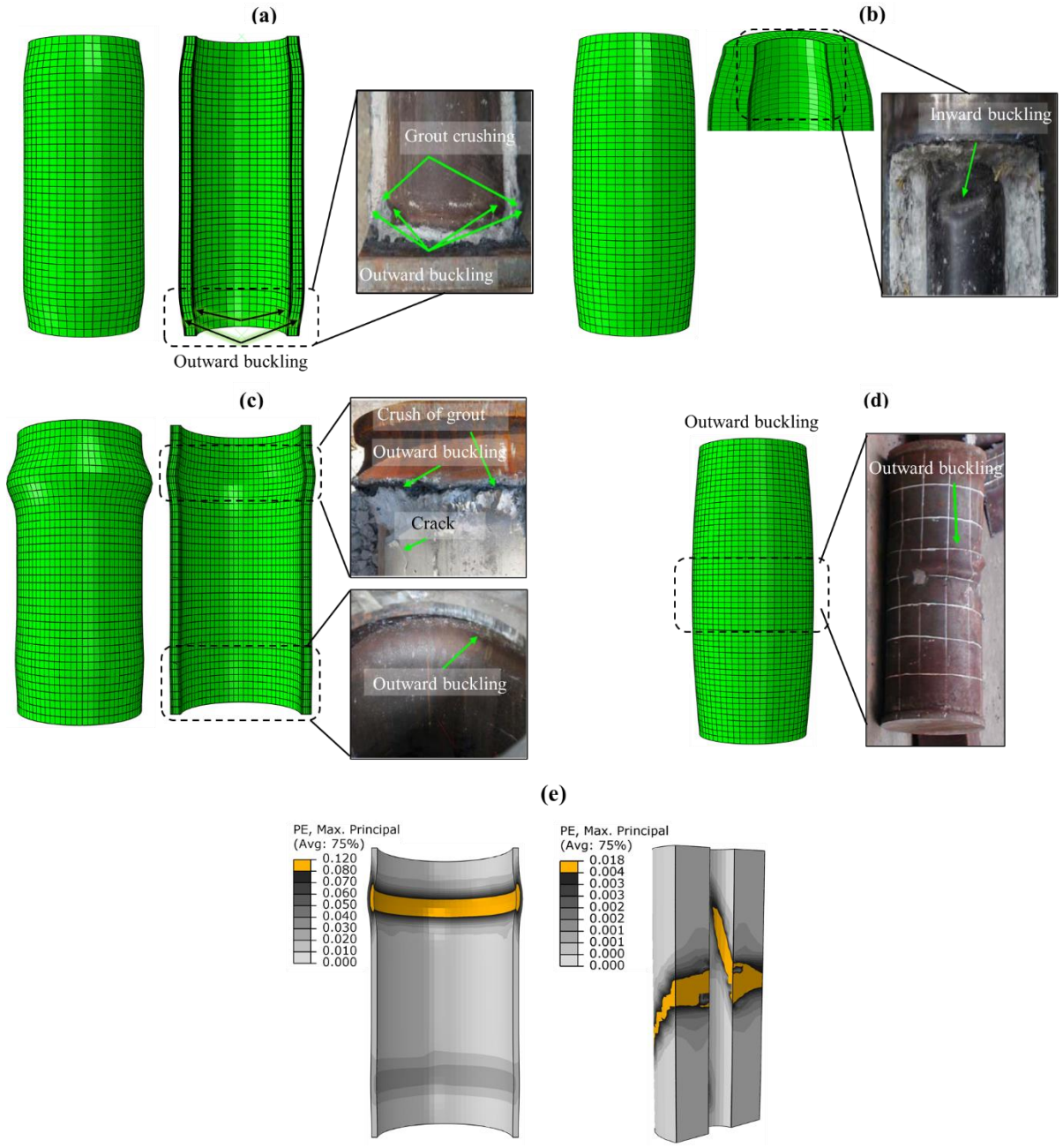

Figure 6: Failure mode comparison between experiments and FE models for tests a) GC1-2, b) GC2-1, c) GCL-1, d) cc3a and infill material crushing for GCL-1 and cc3a

4. Parametric study

Upon successful validation, the numerical models were utilised to conduct an extensive parametric analysis, aiming to investigate the effect of key parameters on the structural response of GFDST stub-columns. The validated models included two cross-sections with external diameters equal to 140 mm and 450 mm. Using these models as a basis, two groups were considered; one with a small (group GCS) and one with a large diameter (group GCL). In order to get an accurate representation of the cross-sectional response, for the numerical models the length of the stub-columns was taken equal to 3 times the external diameter. The effect of the diameter-to-thickness ratio was examined and four

cross-sectional slenderness values equal to 50, 60, 70 and 80 (abbreviated as Dt50, Dt60, Dt70 and Dt80) were investigated for each of the GCS and GCL groups. For the parametric study, the external and internal steel tubes were set to have equal D/t ratios on all FE models and the hollow ratio effect is further investigated in the remaining sections.

4.1 Cross-sectional slenderness

For each one of the D/t values, six hollow ratio values ranging from 0.4 to 0.9 with a step of 0.1 were considered. By maintaining a constant diameter to thickness ratio for both the external and the internal steel tube, the same hollow ratio value χ can be achieved by either varying the diameter and the thickness of the outer tube and keeping the inner tube dimensions constant or vice versa. Both cases have been investigated and are designated as I (followed by the χ value) or O (followed by the χ value), depending on whether the inner or outer tube dimensions have been modified. Adopting the same assumptions described in Section 2, a total of 96 nonlinear analyses were carried out and the results are reported in this section.

The full load-displacement path was captured during the analysis and typical cases for a small scale and a large scale stub column with D/t=60 are shown in Figure 7a and Figure 7b respectively. Note that for the cases with flat load-displacement post-elastic response, where a clear peak value was not observed, the maximum load that was recorded during the simulation was considered to be the ultimate load. In both cases, the effect of the change in the hollow ratio value is evident. In Figure 7a the inner steel tube has been kept constant, while in Figure 7b, the outer steel tube geometric properties are constant for the examined hollow ratios. As anticipated, a smaller hollow ratio that corresponds to a larger grout thickness increases the axial capacity the GFDST stub-column. This is more pronounced in Figure 7a where the outer tube has been modified indicating that the influence of the external steel tube is higher. In most cases, the overall response does not present a sudden loss of strength but rather a stable ductile post-peak response, which is similar to the behaviour reported in the experiments (see Figure 5).

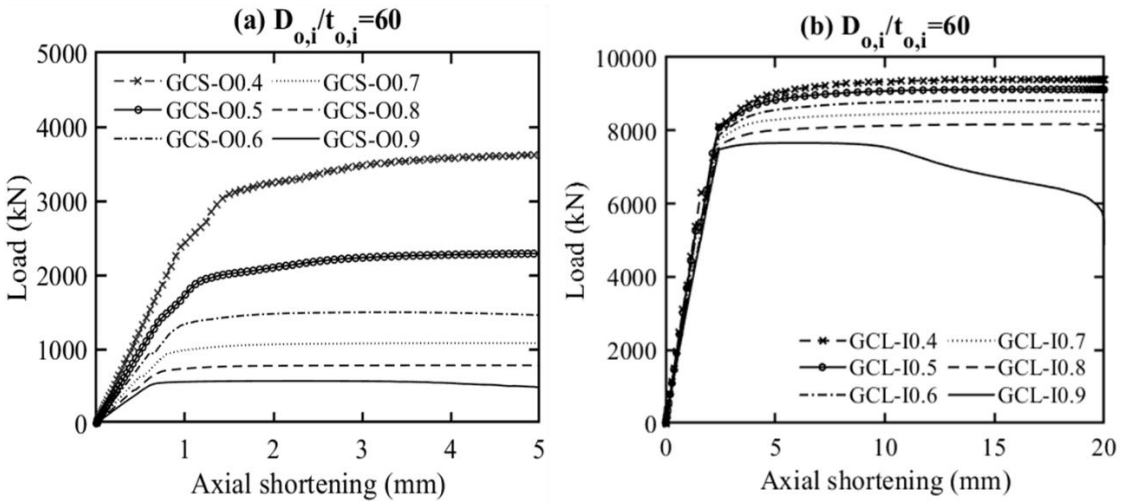

Figure 7: Typical load-displacement curves from parametric models for a) varying external tube and b) varying internal tube

In Figure 8 and Figure 9 the numerically obtained failure loads are normalised against the squash load (F_y), and are plotted against the hollow ratio for the small (GCS group) and large diameter (GCL group) FE models respectively. The squash load is defined as the sum of three terms, which are the products of the yield strength and the cross section of the two steel tubes and the product of the compressive strength of the grout with the cross section of the grout. For each group two cases were investigated, one with a constant outer steel tube and one with a constant inner steel tube. As previously observed in Figure 7, an increase in the value of hollow ratio, decreases the normalised compressive strength of the stub column for all the considered models of the GCS group (Figure 8a, b). The same conclusions are also drawn from the FE models in the GCL group specimens for constant outer and inner tubes, as shown in Figure 9a and Figure 9b respectively. In particular, for GCS with constant external tube, the normalised load was in the range of 1.28 to 1.05 for hollow ratio equal to 0.4 and 0.9, respectively. The same ratios were equal to 1.29 to 1.02 for GCS with constant inner tube, 1.36 to 1.03 for GCL with constant external tube and 1.29 to 1.04 for GCL with constant inner tube. In addition, no clear effect of the D/t value on the normalised load was observed.

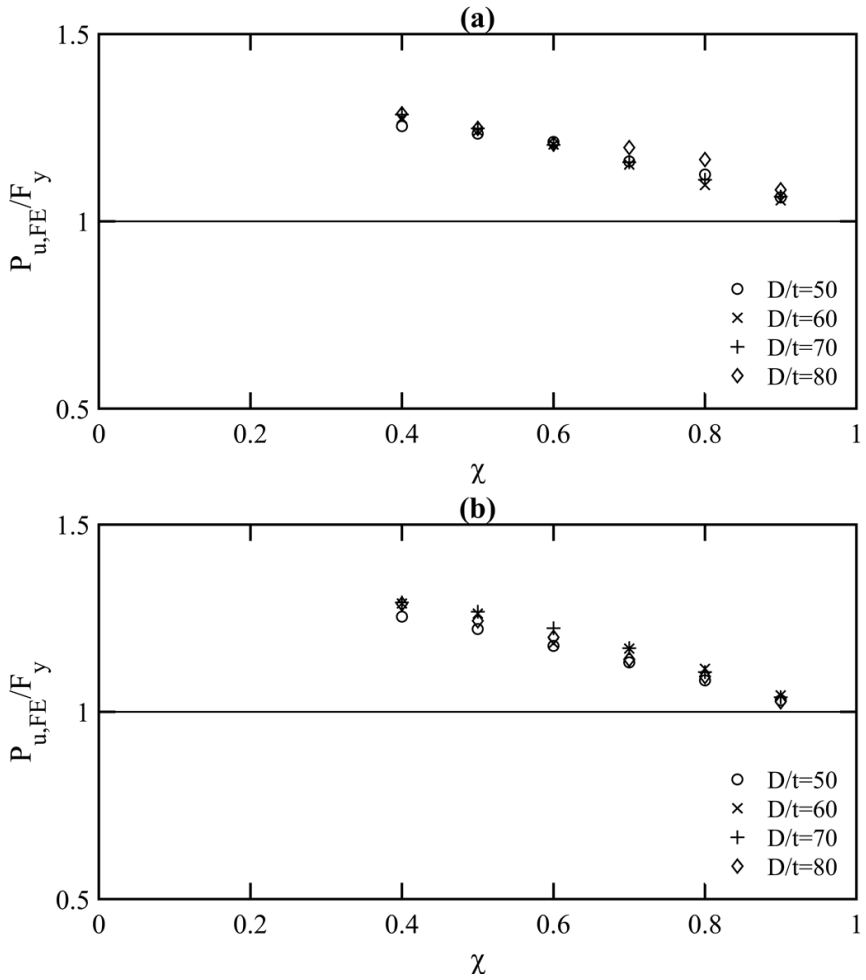

Figure 8: Effect of steel tube cross section on the axial compressive strength of FE models in group GCS for a) constant external tube and b) constant inner tube

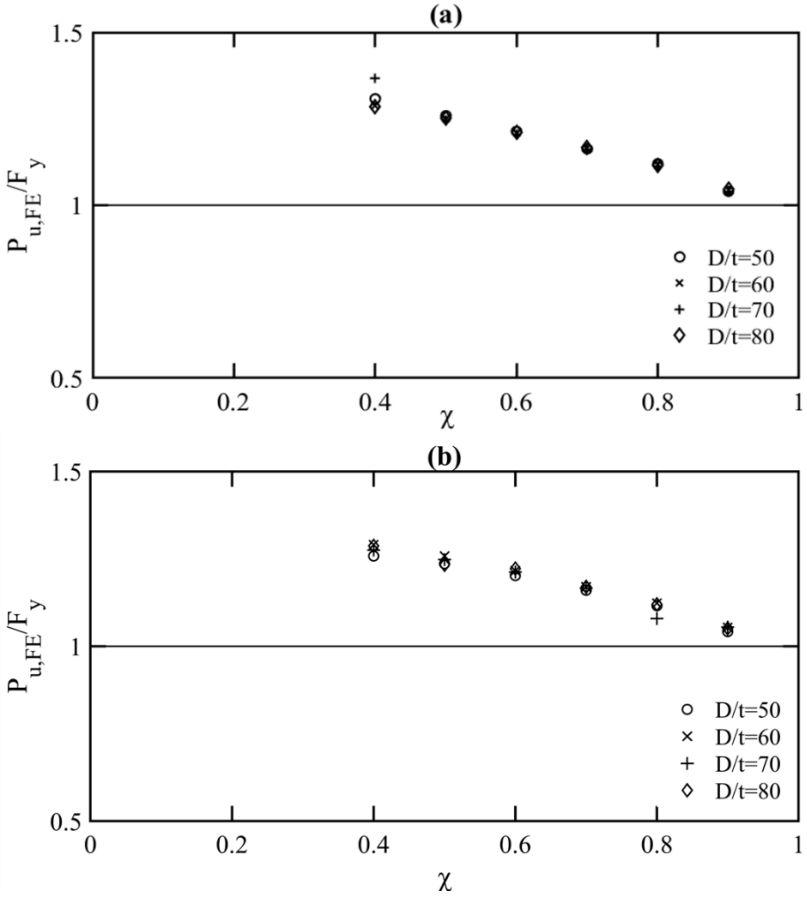

Figure 9: Effect of steel tube cross section on the axial compressive strength of FE models in group GCL for a) constant external tube and b) constant inner tube

4.2 Effect of grout thickness

For the GCS group with D/t=80, the axial stresses for increasing grout thickness are visualised in Figure 10. The grout thicknesses at Figures 10(a) to 10(d) were 6.35 mm, 24.51 mm , 38.13 mm and 85.81 mm and the corresponding ultimate loads P_u were 436.99 kN, 871.11 kN, 1260.64 kN, 3099,45 kN respectively. In all cases, the bottom cross-section shows the stress distribution in N/mm^2 when the failure load (P_u) was reached and the top cross section shows the stresses at P=0.25P_u, during the elastic stage of the load-axial shortening curve. For the examined FE models, the stresses on the grout core indicate a smooth transition along the thickness during the elastic stage. For example for the models with intermediate thicknesses (see Figure 10(b) and (c)), the stresses appear to be in the range of 7 to 10 N/mm^2 and 8 to 12 N/mm^2 for 0.25 P_u, respectively. Similar are the conclusions for the specimens with higher and lower grout thickness.

On the contrary, once the ultimate load is reached the distribution of stresses from the inner to the outer steel tube, is significantly higher for all models. For example as shown in Figure 10(d), the concrete stresses closer to the inner tube are as low as 9 N/mm^2 and reach values as high as 61 N/mm^2 once closer to the external tube, demonstrating an increase of 52 N/mm^2 towards the outer tube. Similar

is the range for all four cases of Figure 10 with an axial stress range within 48 - 57 N/mm^2. This is owing to the larger confinement that is provided on the grout core from the external steel tube when compared to the internal tube. This is also in agreement with findings presented in section 4.1.

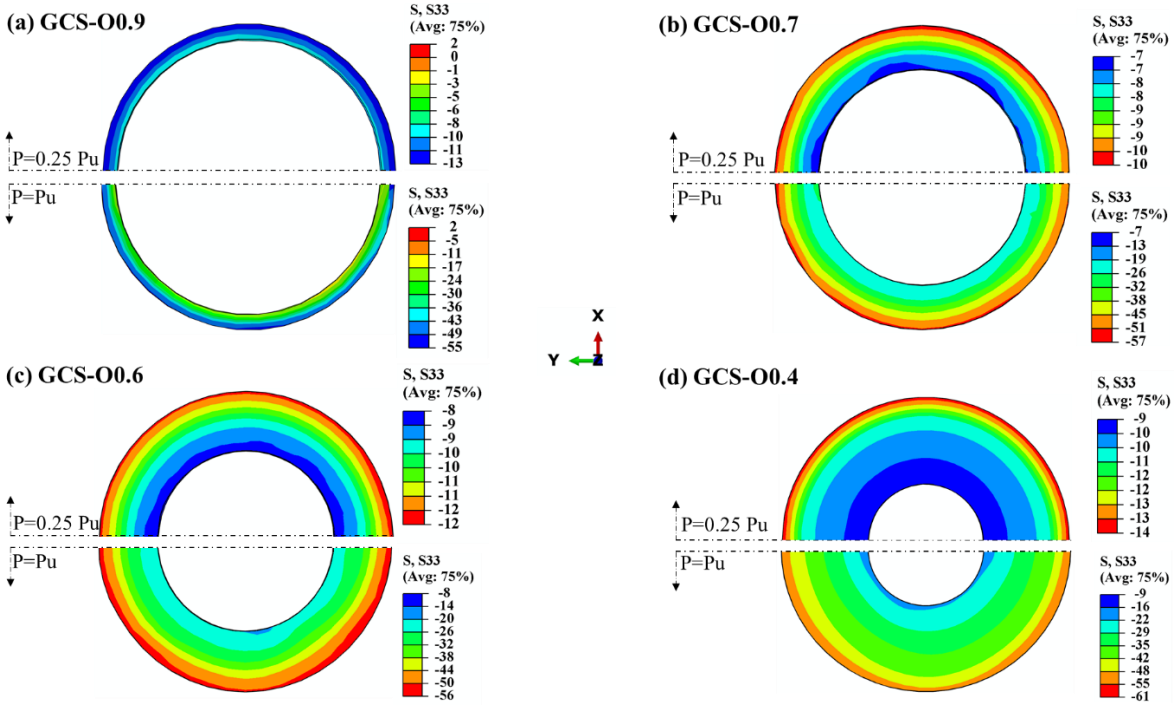

Figure 10: Distribution of stresses on concrete core for varying hollow ratio and constant D/t=80

Typical failure modes that were observed in the numerical models are shown in Figure 11. For sections with large hollow ratio values – hence, small grout core thickness, the lateral restraint was less pronounced, leading to local instabilities at locations where higher compressive steel stresses occurred, as shown in Figure 11a. As it can be observed in Figure 11b and Figure 11c, for Dt60 and Dt70 the compressive stresses led to a local instability in the external steel tube, resulting in a failure mode similar to "elephant foot" buckling. For larger grout thicknesses (Figure 11d), material yielding was the prominent failure mode. Finally, it is noted that the deformed shape of the model shown in Figure 11a corresponds to high applied deformations, well beyond the ultimate load. It is believed that despite the symmetry in terms of geometry, loading and boundary conditions, a non-symmetric deformed shape can occur either as the result numerical instabilities/roundoff errors that start off as infinitesimal but propagate and accumulate throughout the analysis thus becoming significant or due to the bifurcation of the symmetric solution to non-symmetric ones. This secondary bifurcation has been observed experimentally [48] and discussed analytically [49] for circular tubes in compression and it is believed that it can occur for the type of structures studied herein, albeit, the presence of concrete infill makes the switching from an axisymmetric model to a non-axisymmetric one more difficult.

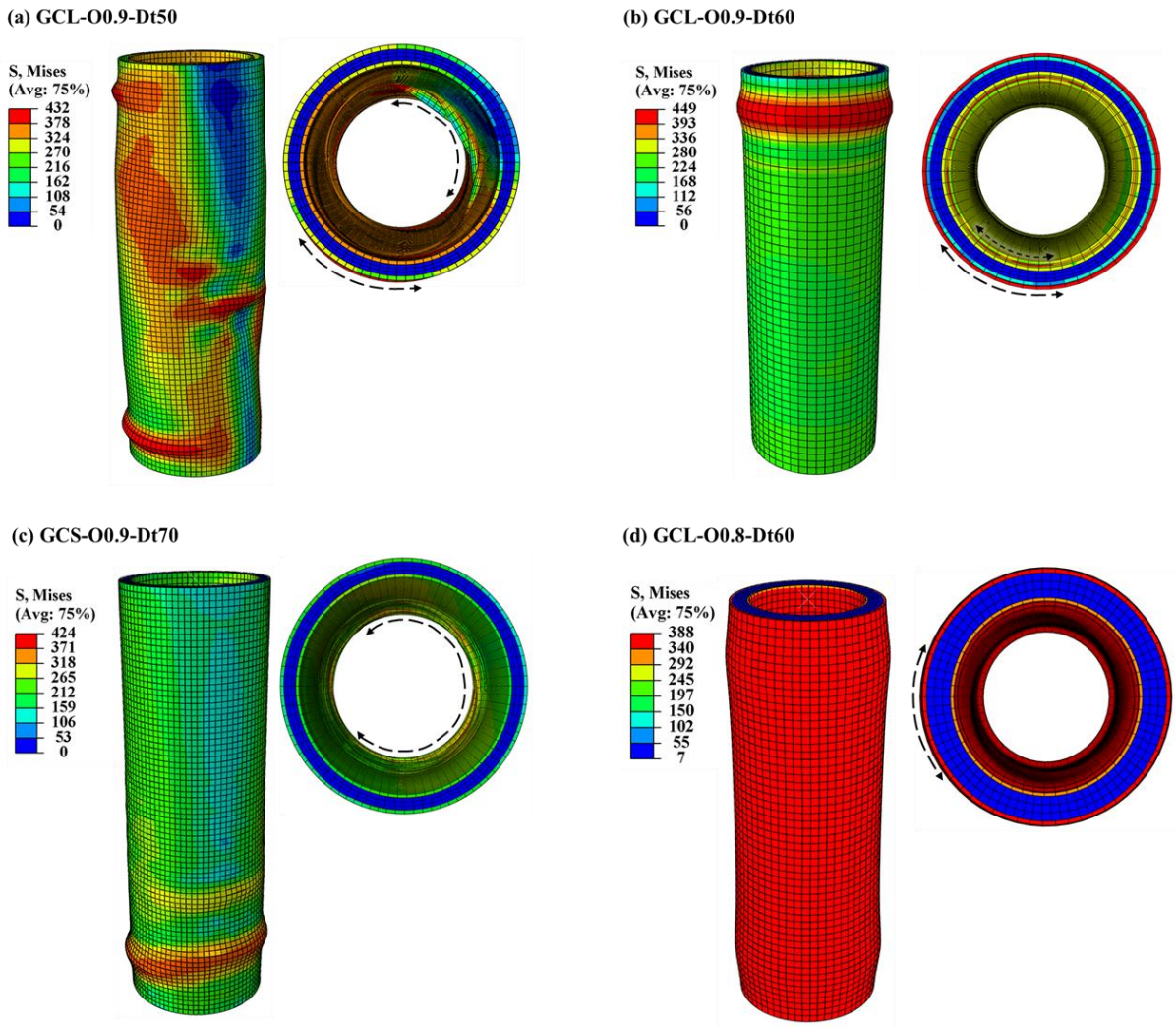

Figure 11: Typical failure modes from FE models for varying cross-sectional slenderness

5 Design Predictions

The data generated from the parametric study alongside experimental data collected from the literature, were employed to assess previously proposed design equations and code specifications and their applicability to GFDST stub-columns. For this purpose, the design equations provided in EC4 [36] and in the ACI code [37] for concrete filled members are modified to be applicable for double-skin tubular steel members and assessed herein. In addition, the analytical models proposed in [8] and [38] are also evaluated. The accuracy of the aforementioned four different design approaches to accurately predict the resistance of double skin cross-sections in compression at ultimate limit state has been assessed.

In sections 5.1-5.4, the design equations that were used, along with the modifications made are presented in detail. The presently generated numerical data along with literature collated data are summarised and compared to the design guidelines in section 5.5.

5.1 Eurocode 4 (EN 1994-1-1)

EN 1994-1-1 (EC4) [36] provides general rules for the design of composite steel-concrete columns and composite structures in compression. Even though the plastic resistance of concrete-filled tubes in compression is detailed in Section 6.7.3.2 [36], the design of filled double-skin steel members is not currently covered by Eurocodes, thus a modification to existing methods was made. EC4 provides a design equation for concrete-filled steel tubes with reinforcement by means of a resistance function. The plastic resistance in compression $N_{pl,Rd}$ is the summation of the resistance of the components forming the cross-section under investigation. The latter has been modified for GFDSTs to include the grout infill and the internal steel tube replaces the steel reinforcement as per equation (14). Similar modifications to EC4 have been employed by Wang et al. [27], for double-skinned sections formed by stainless and high strength steel tubes.

$$P_{EC4}=\eta_a A_{so} f_{syo}+A_g f_c\left(1+\eta_c \frac{t_o}{D_o}\frac{f_{syo}}{f_c}\right)+A_{si} f_{syi} \tag{14}$$

where f_c is the compressive cylinder strength of the grout and, η_a η_c and are given by equations (15) and (16),

$$\eta_a=0.25\left(3+2\bar{\lambda}\right)\leq 1.0 \tag{15}$$

$$\eta_c=4.9-18.5\bar{\lambda}+17\bar{\lambda}^2\geq 0 \tag{16}$$

where $\bar{\lambda}$ is the relative slenderness as described in equation (17):

$$\bar{\lambda}=\sqrt{\frac{N_{pl,Rk}}{N_{cr}}} \tag{17}$$

where $N_{pl,Rk}$ is the characteristic value of the plastic resistance to compression given by equation (18) and evaluated as a sum of forces of the constituent elements. For the grout core a unity coefficient has been employed to take into consideration the confinement effects.

$$N_{pl,Rk}=A_{so} f_{syo}+A_g f_c+A_{si} f_{syi} \tag{18}$$

The elastic critical buckling load (N_{cr}), is calculated with the elastic effective stiffness (EI_{eff}), according to equation (19),

$$EI_{eff}=E_{so} I_{so}+E_{si} I_{si}+K_e E_g I_g \tag{19}$$

where K_e is a correction factor for the grout core equal to 0.6, E the Young's modulus and the second moment of area (I) for each of the components of the cross-section. According to EC 4, for circular hollow steel sections if the local slenderness limit as defined in (20) is exceeded, local buckling ought to be accounted for,

$$D/t \leq 90\left(235/f_{sy}\right) \tag{20}$$

For this reason for the subsequent EC4 calculation, the cross section of the steel tubes was modified to account for local buckling according to equation (21) proposed in [50] and has been recently employed by Wang et al. [27], for CFDST stub-columns with external stainless steel tube.

$$A_{seo,i}=A_{so,i}\left(\frac{90}{D_{o,i}/t_{o,i}}\frac{235}{f_{syo,i}}\frac{E_{o,i}}{210000}\right)^{0.5} \tag{21}$$

where, the subscripts (o, i) refer to the external and internal steel tube.

5.2 American Concrete Institute (ACI)

ACI [37] which is the American code for the design of concrete structures provides design formula for the evaluation of the ultimate strength of concrete-filled circular short columns. Incorporating the contribution of the inner tube, the compressive cross-sectional strength (P_{ACI}) of concrete-filled tubes is modified to equation (22) as follows:

$$P_{ACI}=A_{so}f_{syo}+0.85A_g f_c+A_{si}f_{syi} \tag{22}$$

5.3 Han et al. [8]

Han et al. carried out a series of experiments on CFDST stub columns and proposed a new design equation (23) for the ultimate strength of CFDST cross-sections, also considering the confinement offered to the core from the external steel tube and the influence of the hollow ratio:

$$P_{Han}=A_{sco}f_{scyo}+A_{si}f_{syi} \tag{23}$$

The first term corresponds to the compressive capacity of the external steel tube alongside the sandwiched grout and the second term to the compressive capacity of the internal steel tube. The cross-sectional area A_{sco}, is given from equation (24)

$$A_{sco}=A_{so}+A_g \tag{24}$$

and f_{scyo} is given by equation (25),

$$f_{scyo}=k_1 C_1 \chi^2 f_{syo}+C_2(1.14+1.02\xi)f_c \tag{25}$$

where the coefficients C_1, C_2 and the confinement factor (ξ) are calculated according to equations (26) and (27):

$$C_1=\frac{a}{1+a},\ C_2=\frac{1+a_n}{1+a} \tag{26}$$

$$\xi = a_n \frac{f_{scyo}}{f_c} \quad (27)$$

where a and a_n are the steel ratio and the nominal steel ratio as follows:

$$a = \frac{A_{so}}{A_g}, \; a_n = \frac{A_{so}}{A_{g,nom}} \quad (28)$$

where the nominal cross-section of the sandwiched grout ($A_{g,nom}$) is:

$$A_{g,nom} = \frac{\pi(D_o - 2t_o)^2}{4} \quad (29)$$

5.4 Yu et al. [38]

Yu et al. proposed a unified equation for the estimate of ultimate compressive strength of concrete-filled tubes in compression. To include the internal steel tube, the modification suggested in Hassanein and Kharoob [10] is used herein following Equation (30),

$$P_{Yu,mod} = \left(A_{so} f_{syo} + A_g f_c\right)\left(1 + 0.5\frac{\xi}{1+\xi}\Omega\right) + A_{si} f_{syi} \quad (30)$$

where the solid ratio, Ω is defined as per equation (31), A_k the hollow area as depicted in Figure 1 and the rest as previously defined:

$$\Omega = \frac{A_g}{A_g + A_k} \quad (31)$$

5.5 Assessment of design predictions

In order to evaluate the suitability of design prediction methods, the bearing capacity of the FE models is normalised against the analytically-obtained strength predictions (P_{EC4}, P_{ACI}, P_{Han} and $P_{Yu,mod}$) and is shown in a tabulated format for the small (GCS) and large diameter (GCL) groups, in Table 3 and Table 4 respectively. Collated test data from the literature [6, 8, 12, 20, 21], are also employed for assessment purposes and are shown in Table 5 in a similar format, by normalising test results against design predictions. For both groups of the FE models and collated data it is found that the strength predictions are on the safe side with varying levels of conservatism and scatter as shown in Figure 12, where the ultimate sustained load is normalised with the predicted capacity from each design method and presented against the examined hollow ratios. EC4 yielded safe predictions with similar trends for both groups, with an average of 1.136 and 1.113 for GCS and GCL groups respectively. An increasing conservatism with increasing hollow ratio values is observed to be consistent for small and large-diameter models (Figure 12a). The conservatism for high slenderness is possibly attributed to the local buckling limit suggested in [36], which is currently not explicitly defined for double skin filled tubular

414 members, but hollow steel members. In this case local buckling limit was taken equal to class 3 hollow
415 sections, which does not account for the lateral restraint from the infill material.

416 The design predictions from ACI were found to be the most conservative amongst the design
417 methods. Particularly for smaller hollow ratios (0.4-0.6) a high level of conservatism is shown, whereas
418 this reduces for models with large hollow ratios (Figure 12b). In addition, for all the investigated models
419 a high scatter was observed when this method was employed, which can be associated with the fact that
420 ACI does not account for confinement effects. Similar findings were also reported for CFDST stub-
421 columns with external stainless steel tubes in Wang et al. [27]. Predictions obtained from Han et al. [8]
422 were also found on the safe side with a small scatter and an average of 1.076 for GCS and 1.088 for
423 GCL models (Figure 12c). Strength predictions for models with hollow ratios of 0.8 and 0.9 are closer
424 to unity and overall with less conservatism compared to EC4 and ACI. Yu et al. [38] model results in
425 good predictions close to unity with reduced conservatism (Figure 12d) and a coefficient of variation
426 of 0.029 (GCS group) and 0.025 (GCL group). Overall, it is shown that the modified Yu et al. strength
427 predictions are of lower conservatism. Nevertheless, Han et al. and EC4 methods can also be used for
428 design purposes of GFDST members as the vast majority of the models are on the safe side.

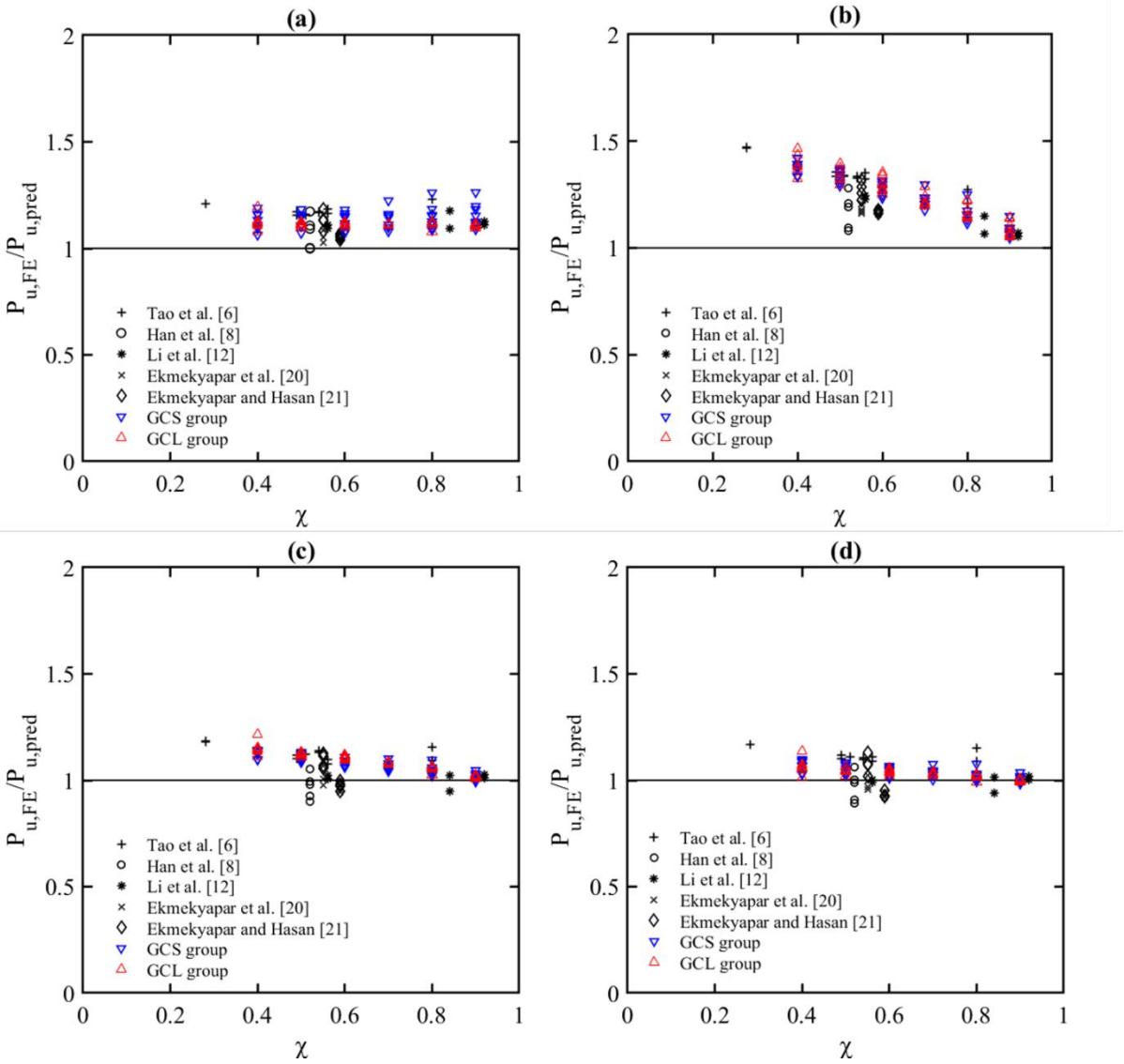

Figure 12: Comparison of FE obtained compressive strength to design strength predictions for small diameter (group GCS) and large diameter (group GCL) models with a) EC4, b) ACI, c) Han et al. [8], d) Yu et al. [38]

Table 3: Comparisons of small diameter FE model with design strength predictions

Group	FE model ID	D/t	D_o (mm)	t_o (mm)	D_i (mm)	t_i (mm)	L (mm)	χ	$\frac{P_{u,EC4}}{P_{u,FE}}$	$\frac{P_{u,ACI}}{P_{u,FE}}$	$\frac{P_{u,Han}}{P_{u,FE}}$	$\frac{P_{u,Yu,mod}}{P_{u,FE}}$
GCS1	I0.9-Dt50	50	140.0	2.80	120.9	2.41	420.0	0.9	1.125	1.080	1.031	1.015
	I0.8-Dt50				107.5	2.15		0.8	1.126	1.156	1.060	1.031
	I0.7-Dt50				94.0	1.88		0.7	1.110	1.206	1.067	1.027
	I0.6-Dt50				80.6	1.61		0.6	1.118	1.273	1.092	1.043
	I0.5-Dt50				67.2	1.34		0.5	1.103	1.306	1.093	1.037
	I0.4-Dt50				53.7	1.07		0.4	1.094	1.337	1.096	1.034
	O0.9-Dt50		131.9	2.63	114.0	2.28	395.8	0.9	1.089	1.046	0.998	0.983
	O0.8-Dt50		148.4	2.96			445.3	0.8	1.085	1.114	1.021	0.994
	O0.7-Dt50		169.6	3.39			508.9	0.7	1.079	1.176	1.042	1.002
	O0.6-Dt50		197.9	3.95			593.7	0.6	1.073	1.233	1.061	1.010
	O0.5-Dt50		237.5	4.75			712.5	0.5	1.071	1.290	1.084	1.022
	O0.4-Dt50		296.8	5.93			890.6	0.4	1.063	1.333	1.099	1.028
GCS2	I0.9-Dt60	60	140.0	2.33	121.8	2.03	420.0	0.9	1.118	1.074	1.022	1.008
	I0.8-Dt60				108.2	1.80		0.8	1.096	1.132	1.034	1.008
	I0.7-Dt60				94.7	1.57		0.7	1.098	1.204	1.061	1.026
	I0.6-Dt60				81.2	1.35		0.6	1.106	1.273	1.089	1.045
	I0.5-Dt60				67.6	1.12		0.5	1.106	1.323	1.105	1.055
	I0.4-Dt60				54.1	0.90		0.4	1.110	1.370	1.122	1.066
	O0.9-Dt60		131.0	2.18	114	1.90	393.1	0.9	1.106	1.062	1.010	0.997
	O0.8-Dt60		147.4	2.45			442.2	0.8	1.113	1.150	1.050	1.024
	O0.7-Dt60		168.4	2.80			505.4	0.7	1.111	1.221	1.077	1.040
	O0.6-Dt60		196.5	3.27			589.6	0.6	1.078	1.248	1.071	1.025
	O0.5-Dt60		235.8	3.93			707.5	0.5	1.108	1.342	1.126	1.068
	O0.4-Dt60		294.8	4.91			884.4	0.4	1.096	1.379	1.137	1.070
GCS3	I0.9-Dt70	70	140.0	2.00	122.4	1.74	420.0	0.9	1.183	1.094	1.031	1.019
	I0.8-Dt70				108.8	1.55		0.8	1.156	1.157	1.046	1.024
	I0.7-Dt70				95.2	1.36		0.7	1.145	1.220	1.067	1.036
	I0.6-Dt70				81.6	1.16		0.6	1.146	1.283	1.090	1.053
	I0.5-Dt70				68.0	0.97		0.5	1.151	1.341	1.114	1.071
	I0.4-Dt70				54.4	0.77		0.4	1.157	1.390	1.134	1.086
	O0.9-Dt70		130.3	1.86	114	1.62	391.1	0.9	1.153	1.066	1.005	0.993
	O0.8-Dt70		146.6	2.09			440.0	0.8	1.151	1.152	1.042	1.020
	O0.7-Dt70		167.6	2.39			502.9	0.7	1.153	1.232	1.079	1.046
	O0.6-Dt70		195.5	2.79			586.7	0.6	1.152	1.297	1.109	1.067
	O0.5-Dt70		234.7	3.35			704.1	0.5	1.148	1.358	1.133	1.083
	O0.4-Dt70		293.3	4.19			880.1	0.4	1.133	1.393	1.143	1.085
GCS4	I0.9-Dt80	80	140.0	1.75	122.8	1.53	420.0	0.9	1.263	1.149	1.047	1.037
	I0.8-Dt80				109.2	1.36		0.8	1.261	1.250	1.096	1.077
	I0.7-Dt80				95.5	1.19		0.7	1.224	1.297	1.102	1.076
	I0.6-Dt80				81.9	1.02		0.6	1.181	1.317	1.092	1.061
	I0.5-Dt80				68.2	0.85		0.5	1.183	1.373	1.116	1.080
	I0.4-Dt80				54.6	0.68		0.4	1.190	1.422	1.139	1.099
	O0.9-Dt80		129.9	1.62	114.0	1.42	389.7	0.9	1.198	1.090	0.993	0.983
	O0.8-Dt80		146.1	1.82			438.4	0.8	1.184	1.174	1.030	1.011
	O0.7-Dt80		167.0	2.08			501.0	0.7	1.161	1.236	1.050	1.025
	O0.6-Dt80		194.8	2.43			584.6	0.6	1.164	1.309	1.088	1.053
	O0.5-Dt80		233.8	2.92			701.5	0.5	1.159	1.364	1.114	1.071
	O0.4-Dt80		292.3	3.65			876.9	0.4	1.161	1.420	1.143	1.093
	Average								**1.136**	**1.244**	**1.076**	**1.040**
	COV								**0.040**	**0.085**	**0.038**	**0.029**

434 Table 4: Comparisons of large diameter FE model with design strength predictions

Group	FE model ID	D/t	D_o (mm)	t_o (mm)	D_i (mm)	t_i (mm)	L (mm)	χ	$\frac{P_{u,EC4}}{P_{u,FE}}$	$\frac{P_{u,ACI}}{P_{u,FE}}$	$\frac{P_{u,Han}}{P_{u,FE}}$	$\frac{P_{u,Yu,mod}}{P_{u,FE}}$
GCL1	I0.9-Dt50	50	450.0	9.00	388.8	7.77	1350.0	0.9	1.101	1.052	1.010	0.990
	I0.8-Dt50				345.6	6.91		0.8	1.121	1.145	1.061	1.021
	I0.7-Dt50				302.4	6.04		0.7	1.111	1.201	1.077	1.021
	I0.6-Dt50				259.2	5.18		0.6	1.113	1.265	1.102	1.032
	I0.5-Dt50				216.0	4.32		0.5	1.116	1.322	1.124	1.042
	I0.4-Dt50				172.8	3.45		0.4	1.128	1.383	1.153	1.060
	O0.9-Dt50		462.9	9.25	400.0	8.00	1388.9	0.9	1.103	1.054	1.012	0.992
	O0.8-Dt50		520.8	10.41			1562.5	0.8	1.118	1.141	1.057	1.017
	O0.7-Dt50		595.2	11.90			1785.7	0.7	1.107	1.197	1.075	1.018
	O0.6-Dt50		694.4	13.88			2083.3	0.6	1.100	1.250	1.093	1.020
	O0.5-Dt50		833.3	16.66			2500.0	0.5	1.093	1.295	1.107	1.020
	O0.4-Dt50		1041.7	20.83			3125.0	0.4	1.079	1.325	1.111	1.012
GCL2	I0.9-Dt60	60	450.0	7.50	391.5	6.52	1350.0	0.9	1.136	1.059	1.015	0.996
	I0.8-Dt60				348.0	5.80		0.8	1.145	1.147	1.060	1.022
	I0.7-Dt60				304.5	5.07		0.7	1.135	1.209	1.081	1.028
	I0.6-Dt60				261.0	4.35		0.6	1.130	1.267	1.101	1.036
	I0.5-Dt60				217.5	3.62		0.5	1.129	1.321	1.122	1.046
	I0.4-Dt60				174.0	2.90		0.4	1.132	1.369	1.141	1.056
	O0.9-Dt60		459.77	7.66	400.0	6.66	1379.3	0.9	1.146	1.068	1.024	1.004
	O0.8-Dt60		517.24	8.62			1551.7	0.8	1.150	1.152	1.065	1.026
	O0.7-Dt60		591.13	9.85			1773.4	0.7	1.140	1.214	1.087	1.032
	O0.6-Dt60		689.65	11.49			2068.9	0.6	1.135	1.273	1.110	1.040
	O0.5-Dt60		827.58	13.79			2482.8	0.5	1.134	1.326	1.132	1.048
	O0.4-Dt60		1034.48	17.24			3103.4	0.4	1.129	1.368	1.147	1.051
GCL3	I0.9-Dt70	70	450.0	6.42	393.4	5.62	1350.0	0.9	1.200	1.085	1.008	0.990
	I0.8-Dt70				349.7	4.99		0.8	1.198	1.175	1.054	1.019
	I0.7-Dt70				306.0	4.37		0.7	1.182	1.240	1.079	1.030
	I0.6-Dt70				262.2	3.74		0.6	1.170	1.297	1.100	1.040
	I0.5-Dt70				218.5	3.12		0.5	1.166	1.350	1.121	1.051
	I0.4-Dt70				174.8	2.49		0.4	1.195	1.464	1.217	1.135
	O0.9-Dt70		457.5	6.53	400.0	5.71	1372.5	0.9	1.220	1.103	1.025	1.006
	O0.8-Dt70		514.7	7.35			1544.1	0.8	1.163	1.140	1.024	0.989
	O0.7-Dt70		588.2	8.40			1764.7	0.7	1.186	1.243	1.084	1.033
	O0.6-Dt70		686.2	9.80			2058.8	0.6	1.176	1.303	1.108	1.044
	O0.5-Dt70		823.5	11.76			2470.5	0.5	1.166	1.350	1.126	1.049
	O0.4-Dt70		1029.4	14.70			3088.2	0.4	1.154	1.385	1.138	1.050
GCL4	I0.9-Dt80	80	450.0	5.62	394.8	4.93	1350.0	0.9	1.273	1.136	1.017	0.999
	I0.8-Dt80				351.0	4.38		0.8	1.250	1.220	1.056	1.024
	I0.7-Dt80				307.1	3.83		0.7	1.229	1.287	1.085	1.040
	I0.6-Dt80				263.2	3.29		0.6	1.211	1.342	1.106	1.051
	I0.5-Dt80				219.3	2.74		0.5	1.204	1.395	1.128	1.065
	I0.4-Dt80				175.5	2.19		0.4	1.199	1.437	1.145	1.075
	O0.9-Dt80		455.8	5.69	400.0	5.00	1367.5	0.9	1.279	1.141	1.021	1.004
	O0.8-Dt80		512.8	1.82			1538.4	0.8	1.256	1.225	1.062	1.029
	O0.7-Dt80		586.0	2.08			1758.2	0.7	1.231	1.289	1.088	1.041
	O0.6-Dt80		683.7	2.43			2051.2	0.6	1.222	1.353	1.118	1.058
	O0.5-Dt80		820.5	10.25			2461.5	0.5	1.185	1.373	1.114	1.045
	O0.4-Dt80		1025.6	12.82			3076.9	0.4	1.196	1.437	1.151	1.070
	Average								**1.113**	**1.231**	**1.088**	**1.033**
	COV								**0.014**	**0.088**	**0.042**	**0.025**

435 Table 5: Comparisons of collated test data with design strength predictions

Source	Test ID	$\frac{P_{u,EC4}}{P_{u,Test}}$	$\frac{P_{u,ACI}}{P_{u,Test}}$	$\frac{P_{u,Han}}{P_{u,Test}}$	$\frac{P_{u,Yu,mod}}{P_{u,Test}}$
[6]	cc2a, cc2b, cc3a, cc3b, cc4a, cc4b, cc5a, cc5b, cc6a, cc6b, cc7a, cc7b	1.179	1.344	1.127	1.118
[8]	DC-1, DC-2. DCc-0, DCc-1, DCc-2	1.074	1.171	0.970	0.971
[12]	GC1-1, GC1-2, GC2-1, GC2-2, GCL-1, GCL-2	1.118	1.135	1.006	0.995
[20]	0-1-1-1, 0-1-1-2, 0-2-1-1, 0-2-1-2, 0-2-1-2, 0-1-2-1, 0-1-2-2, 0-2-2-1, 0-2-2-2	1.053	1.175	0.991	0.959
[21]	1-1-2, 2-1-2, 1-1-1, 2-1-1, 1-2-2, 2-2-2, 1-2-1, 2-2-1	1.095	1.221	1.033	1.007
	Average	**1.113**	**1.230**	**1.041**	**1.025**
	COV	**0.055**	**0.082**	**0.071**	**0.078**

436 In Figure 13, the ultimate capacity obtained from the collated test data or the presented FE models is
437 normalised against the plastic resistance design predictions from EC4 and ACI. In this case buckling of
438 the slender cross-sections is not considered, thus allowing to examine the applicability of the class 3
439 limit for GFDST stub-columns. The current limits for local buckling are also plotted for each design
440 method.

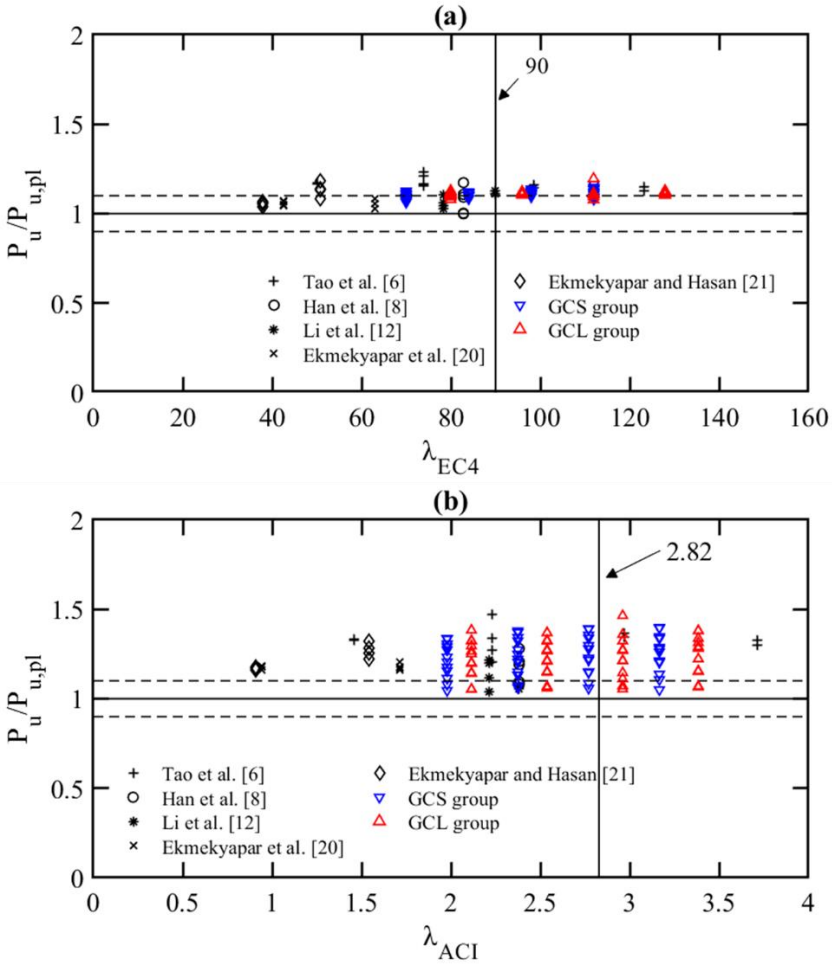

441

442 Figure 13 : Comparison of collated experimental data and FE models against strength predictions from a) EC4
443 and b) ACI

In Figure 13a, it is shown that strength predictions are on the safe side for GCS, GCL groups and also for the experimental data, hence it is suggested that further investigations are required to define a more appropriate slenderness limit for GFDST stub-columns, considering the lateral restraint provided by the infill material. This could potentially result in strength predictions with less conservatism. The ACI model, despite the ease of use resulted in very large scatter and conservatism for all the investigated data (Figure 13b). Considering local buckling improved the results as shown in Figure 12b, however further fine tuning of the model is required in order to consider confinement effects for varying cross-sections and strain hardening of steel tubes, to allow for less conservative results.

6 Conclusions

A comprehensive numerical investigation on the behaviour of tubular GFDST stub-columns was presented in this paper. The numerical models have been validated against experimental data from the literature, replicating the experimentally observed the load-displacement performance, the failure modes and the load capacity. A detailed description of the numerical considerations and assumptions was given and a parametric study, aiming to generate additional structural performance data and to evaluate the influence of key parameters has been carried out. The following conclusions were drawn:

- It was shown that the compressive capacity of GFDST stub-columns increases as the hollow ratio decreases. In most cases the GFDST stub-columns failed in a ductile manner once the peak load was reached.
- An investigation on the distribution of stresses laterally across the cross section of the examined models, showed that higher stresses occur close to the external steel tube for GFDSTs at ultimate capacity. This suggests that the confinement effect offered by the internal steel tube may be less pronounced for double skin sections.
- The modified design method of EC4 showed good strength predictions for both groups and is suggested that it may be employed for the design of GFDST stub-columns, however further studies are required to define an appropriate slenderness limit. On the contrary, ACI yielded the higher levels of conservatism, especially for hollow ratios between 0.4 and 0.6.
- Han et al. and the modified Yu et al. models produced good strength predictions with lower conservatism. Overall, Yu et al. results were superior to other methods with the smallest coefficient of variation for all groups. It should be noted that both models were specifically developed for double skin filled stub-columns.

References

[1] Espinos A, Romero ML, Serra E, Hospitaler A. Experimental investigation on the fire behaviour of rectangular and elliptical slender concrete-filled tubular columns. Thin-Walled Struct 2015;93:137–48. https://doi.org/10.1016/j.tws.2015.03.018

[2] Portolés JM, Romero ML, Bonet JL, Filippou FC. Experimental study of high strength concrete-filled circular tubular columns under eccentric loading. J Constr Steel Res 2011;67:623–33. https://doi.org/10.1016/j.jcsr.2010.11.017

[3] Han LH, Li W, Bjorhovde R. Developments and advanced applications of concrete-filled steel tubular (CFST) structures: Members. J Constr Steel Res 2014;100:211–28. https://doi.org/10.1016/j.jcsr.2014.04.016

[4] Vernardos S, Gantes C. Experimental behavior of concrete-filled double-skin steel tubular (CFDST) stub members under axial compression: A comparative review. Structures 2019;22:383–404. https://doi.org/10.1016/j.istruc.2019.06.025

[5] Giakoumelis G, Lam D. Axial capacity of circular concrete-filled tube columns. J Constr Steel Res 2004;60:1049–68. https://doi.org/10.1016/j.jcsr.2003.10.001

[6] Tao Z, Han LH, Zhao XL. Behaviour of concrete-filled double skin (CHS inner and CHS outer) steel tubular stub columns and beam-columns. J Constr Steel Res 2004;60:1129–58. https://doi.org/10.1016/j.jcsr.2003.11.008

[7] Zhao XL, Tong LW, Wang XY. CFDST stub columns subjected to large deformation axial loading. Eng Struct 2010;32:692–703. https://doi.org/10.1016/j.engstruct.2009.11.015

[8] Han LH, Li YJ, Liao FY. Concrete-filled double skin steel tubular (CFDST) columns subjected to long-term sustained loading. Thin-Walled Struct 2011;49:1534–43. https://doi.org/10.1016/j.tws.2011.08.001

[9] Hu HT, Su FC. Nonlinear analysis of short concrete-filled double skin tube columns subjected to axial compressive forces. Mar Struct 2011;24:319–37. https://doi.org/10.1016/j.marstruc.2011.05.001

[10] Hassanein MF, Kharoob OF. Compressive strength of circular concrete-filled double skin tubular short columns. Thin-Walled Struct 2014;77:165–73. https://doi.org/10.1016/j.tws.2013.10.004

[11] Tziavos NI, Hemida H, Dirar S, Papaelias M, Metje N, Baniotopoulos C. Structural health monitoring of grouted connections for offshore wind turbines by means of acoustic emission: An experimental study. Renew Energy 2020;147:130–40. https://doi.org/10.1016/j.renene.2019.08.114

[12] Li W, Wang D, Han LH. Behaviour of grout-filled double skin steel tubes under compression and bending: Experiments. Thin-Walled Struct 2017;116:307–19. https://doi.org/10.1016/j.tws.2017.02.029

[13] Wang FC, Han LH. Analytical behavior of carbon steel-concrete-stainless steel double-skin tube (DST) used in submarine pipeline structure. Mar Struct 2019;63:99–116. https://doi.org/10.1016/j.marstruc.2018.09.001

[14] Patel VI, Liang QQ, Hadi MNS. Numerical analysis of circular double-skin concrete-filled stainless steel tubular short columns under axial loading. Structures 2020;24:754–65. https://doi.org/10.1016/j.istruc.2020.02.001

[15] Liang QQ, Fragomeni S. Nonlinear analysis of circular concrete-filled steel tubular short columns under axial loading. J Constr Steel Res 2009;65:2186–96. https://doi.org/10.1016/j.jcsr.2009.06.015

[16] Han LH, Tao Z, Huang H, Zhao XL. Concrete-filled double skin (SHS outer and CHS inner) steel tubular beam-columns. Thin-Walled Struct 2004;42:1329–55. https://doi.org/10.1016/j.tws.2004.03.017

[17] Uenaka K, Kitoh H, Sonoda K. Concrete filled double skin circular stub columns under compression. Thin-Walled Struct 2010;48:19–24. https://doi.org/10.1016/j.tws.2009.08.001

[18] Wei S, Mau ST, Vipulanandan C, Mantrala SK. Performance of new sandwich tube under axial loading: Experiment. J Struct Eng 1995;121:1806–14. https://doi.org/10.1061/(ASCE)0733-9445(1995)121:12(1806)

[19] Essopjee Y, Dundu M. Performance of concrete-filled double-skin circular tubes in compression. Compos Struct 2015;133:1276–83. https://doi.org/10.1016/j.compstruct.2015.08.033

[20] Ekmekyapar T, Alwan OH, Hasan HG, Shehab BA, AL-Eliwi BJM. Comparison of classical, double skin and double section CFST stub columns: Experiments and design formulations. J Constr Steel Res 2019;155:192–204. https://doi.org/10.1016/j.jcsr.2018.12.025

[21] Ekmekyapar T, Ghanim Hasan H. The influence of the inner steel tube on the compression behaviour of the concrete filled double skin steel tube (CFDST) columns. Mar Struct 2019;66:197–212. https://doi.org/10.1016/j.marstruc.2019.04.006

[22] Zhao XL, Grzebieta R. Strength and ductility of concrete filled double skin (SHS inner and SHS outer) tubes. Thin-Walled Struct 2002;40:199–213. https://doi.org/10.1016/S0263-8231(01)00060-X

[23] Tao Z, Han LH. Behaviour of concrete-filled double skin rectangular steel tubular beam-columns. J Constr Steel Res 2006;62:631–46. https://doi.org/10.1016/j.jcsr.2005.11.008

[24] Han LH, Huang H, Tao Z, Zhao XL. Concrete-filled double skin steel tubular (CFDST) beam-columns subjected to cyclic bending. Eng Struct 2006;28:1698–714. https://doi.org/10.1016/j.engstruct.2006.03.004

539 [25] Aghdamy S, Thambiratnam DP, Dhanasekar M, Saiedi S. Effects of load-related parameters on
540 the response of concrete-filled double-skin steel tube columns subjected to lateral impact. J Constr Steel
541 Res 2017;138:642–62. https://doi.org/10.1016/j.jcsr.2017.08.015

542 [26] Huang H, Han LH, Zhao XL. Investigation on concrete filled double skin steel tubes (CFDSTs)
543 under pure torsion. J Constr Steel Res 2013;90:221–34. https://doi.org/10.1016/j.jcsr.2013.07.035

544 [27] Wang F, Young B, Gardner L. Compressive testing and numerical modelling of concrete-filled
545 double skin CHS with austenitic stainless steel outer tubes. Thin-Walled Struct 2019;141:345–59.
546 https://doi.org/10.1016/j.tws.2019.04.003

547 [28] Wang F, Young B, Gardner L. CFDST sections with square stainless steel outer tubes under axial
548 compression: Experimental investigation, numerical modelling and design. Eng Struct
549 2020;207:110189. https://doi.org/10.1016/j.engstruct.2020.110189

550 [29] Wang F, Young B, Gardner L. Experimental Study of Square and Rectangular CFDST Sections
551 with Stainless Steel Outer Tubes under Axial Compression. J Struct Eng (United States) 2019;145.
552 https://doi.org/10.1061/(ASCE)ST.1943-541X.0002408

553 [30] Zhou F, Young B. Concrete-filled double-skin aluminum circular hollow section stub columns.
554 Thin-Walled Struct 2018;133:141–52. https://doi.org/10.1016/j.tws.2018.09.037

555 [31] Elchalakani M, Hassanein MF, Karrech A, Fawzia S, Yang B, Patel VI. Experimental tests and
556 design of rubberised concrete-filled double skin circular tubular short columns. Structures
557 2018;15:196–210. https://doi.org/10.1016/j.istruc.2018.07.004

558 [32] Pagoulatou M, Sheehan T, Dai XH, Lam D. Finite element analysis on the capacity of circular
559 concrete-filled double-skin steel tubular (CFDST) stub columns. Eng Struct 2014;72:102–12.
560 https://doi.org/10.1016/j.engstruct.2014.04.039

561 [33] Hassanein MF, Elchalakani M, Karrech A, Patel VI, Yang B. Behaviour of Concrete-filled Double-
562 skin Short Columns Under Compression Through Finite Element Modelling: SHS Outer and SHS Inner
563 Tubes. Structures 2018;14:358–75. https://doi.org/10.1016/j.istruc.2018.04.006

564 [34] Ding F xing, Wang W jun, Lu D ren, Liu X mei. Study on the behavior of concrete-filled square
565 double-skin steel tubular stub columns under axial loading. Structures 2020;23:665–76.
566 https://doi.org/10.1016/j.istruc.2019.12.008

567 [35] Duarte APC, Silva BA, Silvestre N, de Brito J, Júlio E, Castro JM. Finite element modelling of
568 short steel tubes filled with rubberized concrete. Compos Struct 2016;150:28–40.
569 https://doi.org/10.1016/J.COMPSTRUCT.2016.04.048

570 [36] EN 1994-1-1, Eurocode 4, Design of Composite Steel and Concrete Structures, Part 1.1: General
571 Rules and Rules for Buildings, European Committee for Standardization (CEN), Brussels, 2004.

572 [37] ACI 318, Building Code Requirements for Structural Concrete and Commentary, Farmington
573 Hills, Michigan, USA, 2014.

574 [38] Yu M, Zha X, Ye J, Li Y. A unified formulation for circle and polygon concrete-filled steel tube
575 columns under axial compression. Eng Struct 2013;49:1–10.
576 https://doi.org/10.1016/j.engstruct.2012.10.018

577 [39] ABAQUS, ABAQUS/standard User's Manual. Version 2019, Dassault Systemes Simulia Corp.,
578 USA, 2019.

579 [40] Wang J, Afshan S, Gkantou M, Theofanous M, Baniotopoulos C, Gardner L. Flexural behaviour
580 of hot-finished high strength steel square and rectangular hollow sections. J Constr Steel Res
581 2016;121:97–109. https://doi.org/10.1016/j.jcsr.2016.01.017

582 [41] Tziavos NI, Hemida H, Metje N, Baniotopoulos C. Non-linear finite element analysis of grouted
583 connections for offshore monopile wind turbines. Ocean Eng 2019;171:633–45.
584 https://doi.org/10.1016/j.oceaneng.2018.11.005

585 [42] Mander JB, Priestley MJ, Park R, Theoretical stress-strain model for confined concrete. J Struct
586 Eng 1988; 114 (8):1804-1826. https://doi:10.1061/(ASCE)0733-9445(1988)114:8(1804)

587 [43] Richart FE, Brandtzaeg A, Brown RL, A study of the failure of concrete under combined
588 compressive stresses. University of Illinois at Urbana Champaign, (1973).

589 [44] Hu HT, Huang CS, Wu MH, Wu YM. Nonlinear analysis of axially loaded concrete-filled tube
590 columns with confinement effect. J Struct Eng 2003;129:1322–9. https://doi.org/10.1061/(ASCE)0733-
591 9445(2003)129:10(1322)

592 [45] Tao Z, Wang Z Bin, Yu Q. Finite element modelling of concrete-filled steel stub columns under
593 axial compression. J Constr Steel Res 2013;89:121–31. https://doi.org/10.1016/j.jcsr.2013.07.001

594 [46] CEB-FIP CE. Model code 2010. Comite Euro-International du beton, 2010.

595 [47] Thai HT, Uy B, Khan M, Tao Z, Mashiri F. Numerical modelling of concrete-filled steel box
596 columns incorporating high strength materials. J Constr Steel Res 2014;102:256–65.
597 https://doi.org/10.1016/j.jcsr.2014.07.014

598 [48] Bardi FC, Kyriakides S. Plastic buckling of circular tubes under axial compression-part I:
599 Experiments. Int J Mech Sci 2006;48:830–41. https://doi.org/10.1016/j.ijmecsci.2006.03.005

600 [49] Bardi FC, Kyriakides S, Yun HD. Plastic buckling of circular tubes under axial compression-part
601 II: Analysis. Int J Mech Sci 2006;48:842–54. https://doi.org/10.1016/j.ijmecsci.2006.03.002

602 [50] Chan TM, Gardner L. Compressive resistance of hot-rolled elliptical hollow sections. Eng Struct
603 2008;30:522–32. https://doi.org/10.1016/j.engstruct.2007.04.019